SCIENTIFIC REPORTS

OPEN

Hybrid Energy Storage of $Ni(OH)_2$-coated N-doped Graphene Aerogel//N-doped Graphene Aerogel for the Replacement of NiCd and NiMH Batteries

Received: 5 January 2017
Accepted: 28 March 2017
Published online: 25 April 2017

Pichamon Sirisinudomkit[1,2], Pawin Iamprasertkun[1], Atiweena Krittayavathananon[1], Tanut Pettong[1], Peerapan Dittanet[2] & Montree Sawangphruk[1]

Although Nickel–Cadmium (NiCd) and Nickel–metal hydride (NiMH) batteries have been widely used, their drawbacks including toxic Cd and expensive La alloy at the negative electrodes, low energy density (40–60 Wh/kg for NiCd and 140–300 Wh/L for NiMH), low power density (150 W/kg for NiCd and 1000 W/kg for NiMH), and low working potential (1.2 V) limit their applications. In this work, Cd and La alloy were replaced with N-doped reduced graphene oxide aerogel (N-rGO$_{ae}$) providing a hybrid energy storage (HES) having the battery and supercapacitor effects. The HES of $Ni(OH)_2$-coated N-rGO$_{ae}$//N-rGO$_{ae}$ provides 1.5 V, a specific energy of 146 Wh/kg, a maximum specific power of 7705 W/kg, and high capacity retention over 84.6% after 5000 cycles. The mass change at the positive electrode during charging/discharging is 8.5 μg cm^{-2} owing to the insertion/desertion of solvated OH^- into the α-$Ni(OH)_2$-coated N-rGO$_{ae}$. At the negative electrode, the mass change of the solvated K^+, physically adsorbed/desorbed to the N-rGO$_{ae}$, is 7.5 μg cm^{-2}. *In situ* X-ray absorption spectroscopy (XAS) shows highly reversible redox reaction of α-$Ni(OH)_2$. The as-fabricated device without using toxic Cd and expensive La alloy has a potential as a candidate of NiCd and NiMH.

Although the Nickel–Cadmium (NiCd) and Nickel–metal hydride (NiMH) batteries have been widely used, their drawbacks including toxic cadmium and expensive lanthanum alloy at the negative electrodes, low energy density (40–60 Wh/kg for NiCd and 140–300 Wh/L for NiMH), low power density (150 W/kg for NiCd and 1000 W/kg for NiMH), and low working potential (1.2 V) limit their applications in electric vehicles, laptops, and mobile phones when compared with Li-ion batteries[1,2]. At the positive electrode, NiOOH and $Ni(OH)_2$ are used for NiCd and NiMH, respectively.

Recently $Ni(OH)_2$-based supercapacitors have also attached a superior attention because of its high theoretical specific capacitance (2,082 F g^{-1})[3,4], affordable price, abundant natural resources, and excellent environment compatibility[4]. More interestingly, some pervious work even reported the remarkably high specific capacitances of $Ni(OH)_2$-based supercapacitors, which are over its theoretical value[5–10]. Generally, α-$Ni(OH)_2$ and β-$Ni(OH)_2$ are the two common phases of $Ni(OH)_2$, which have been using as the supercapacitor electrodes[11]. α-$Ni(OH)_2$/γ-NiOOH redox couple can transform to β-$Ni(OH)_2$/β-NiOOH redox couple easily, which can lead to a specific capacitance decay[12,13]. However, many β-$Ni(OH)_2$-based supercapacitors with great electrochemical performance have still been reported[14–17]. As the results, it needs more understanding in the charge storage mechanism of $Ni(OH)_2$-based supercapacitors. It is also necessary to note here that there is a critic arguing that $Ni(OH)_2$ storing the charges via a phase transformation cannot be considered as the conventional supercapacitor

[1]Department of Chemical and Biomolecular Engineering, School of Energy Science and Engineering, Vidyasirimedhi Institute of Science and Technology, Rayong, 21210, Thailand. [2]Department of Chemical Engineering, Centre for Advanced Studies in Nanotechnology and Its Applications in Chemical Food and Agricultural Industries, and NANOTEC-KU-Centre of Excellence on Nanoscale Materials Design for Green Nanotechnology, Kasetsart University, Bangkok, 10900, Thailand. Correspondence and requests for materials should be addressed to M.S. (email: montree.s@vistec.ac.th)

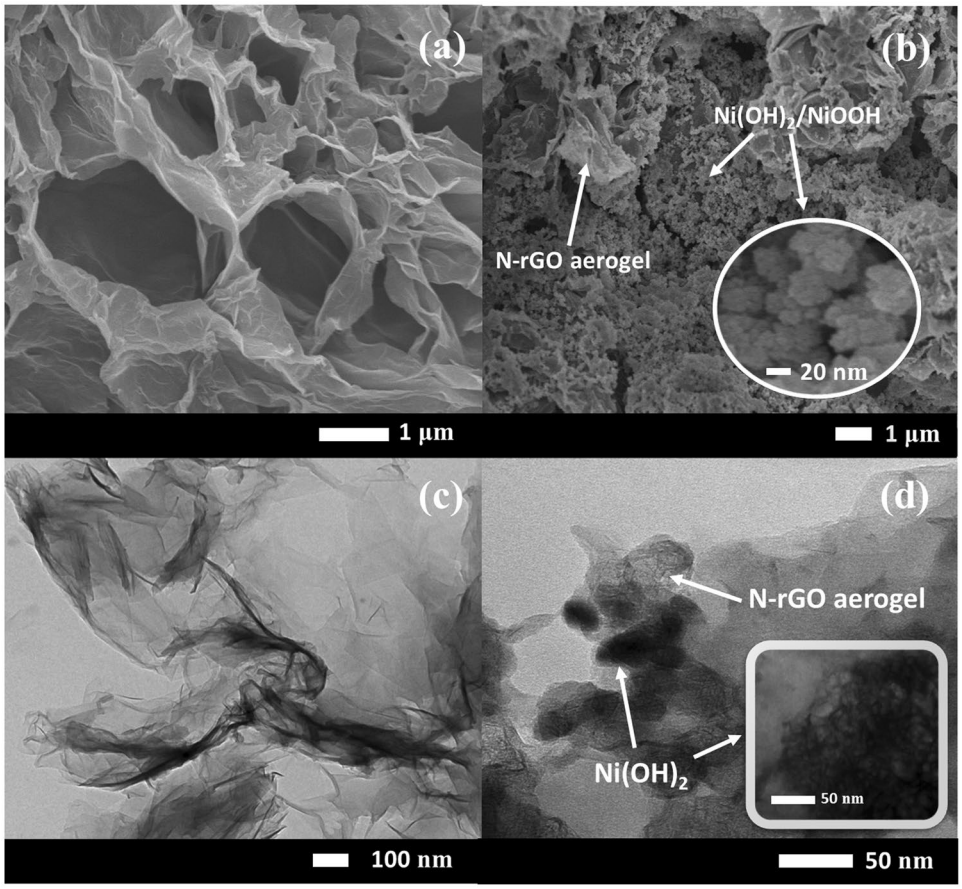

Figure 1. FE-SEM images of (**a**) N-rGO$_{ae}$ spray-coated on CFP, (**b**) Ni(OH)$_2$ electrodeposited on the N-rGO$_{ae}$/CFP. TEM images of (**c**) N-rGO$_{ae}$ and (**d**) Ni(OH)$_2$ coated on N-rGO$_{ae}$.

materials[18,19]. Our results here also show that Ni(OH)$_2$-coated N-doped reduced graphene aerogel (N-rGO$_{ae}$) mainly stores the electronic charge via a bulk redox reaction especially as very slow charging/discharging rates.

Although the reaction mechanism of the Ni(OH)$_2$ itself follows the reversible reaction (1)[20,21], the charge storage mechanism of Ni(OH)$_2$ composites e.g., Ni(OH)$_2$/graphene is not yet clear.

$$\alpha\text{-Ni(OH)}_2 + \text{OH}^- \leftrightarrow \gamma\text{-NiOOH} + \text{H}_2\text{O} + \text{e}^- \quad (1)$$

Note, the reaction (1) originally introduced by Bode *et al.*[1,2] *is well known in NiCd and NiMH batteries*. For the Ni(OH)$_2$ supercapacitors, the theoretical specific capacitance of Ni(OH)$_2$ is based on the reaction (1). However, the electrochemical property of α-Ni(OH)$_2$ is still far lower than its theoretical value due to its insulating property, poor capacity retention and irreversible reaction[22]. To overcome the drawbacks of the Ni(OH)$_2$, it was produced on the conducting graphene sheets providing a specific energy of ca. 37 W h kg^{-1} [3]. In this research, α-Ni(OH)$_2$ is coated on N-rGO$_{ae}$ and used for the asymmetric energy storage (AES) of Ni(OH)$_2$-N-rGO$_{ae}$//N-rGO$_{ae}$ leading to high specific energy and power. This is because N-rGO$_{ae}$ has high electrical conductivity (2×10^3 S cm^{-1})[23], high ionic conductivity due to nitrogen- and oxygen-containing groups and high porosity, which is good for the diffusion of the electrolyte[24,25]. The as-fabricated AES of the Ni(OH)$_2$-coated N-rGO$_{ae}$//N-rGO$_{ae}$ in a CR2016 coin cell can deliver a wide cell working potential up to 1.5 V and high specific energy and maximum specific power of 146 Wh kg^{-1} and 7705 W kg^{-1}, respectively.

In addition, the charge storage mechanisms of both α-Ni(OH)$_2$-coated N-rGO$_{ae}$ and N-rGO$_{ae}$ are investigated in this work by means of *in situ* X-ray absorption spectroscopy (XAS) and *in situ* electrochemical quartz crystal microbalance (EQCM). The result shows that the AES of α-Ni(OH)$_2$-coated N-rGO$_{ae}$//N-rGO$_{ae}$ can store charges via both physical adsorption and redox reaction.

Results and Discussion

Morphologies of the as-synthesised materials. The morphology of the as-synthesized materials was investigated by Field Emission Scanning Electron Microscopy (FE-SEM). The 3D porous network structure of N-rGO$_{ae}$ was coated on flexible carbon fiber paper (CFP) substrate (see Fig. 1a) for which the N-rGO sheets are interconnected each other forming high porosity aerogel. Other physicochemical properties of the N-rGO$_{ae}$ were previously reported by our group elsewhere[26,27]. An FE-SEM image of Ni(OH)$_2$ electrodeposited on the N-rGO$_{ae}$/CFP shows that Ni(OH)$_2$ was fully loaded to the pores of the N-rGO$_{ae}$ and the Ni(OH)$_2$ nanoparticles

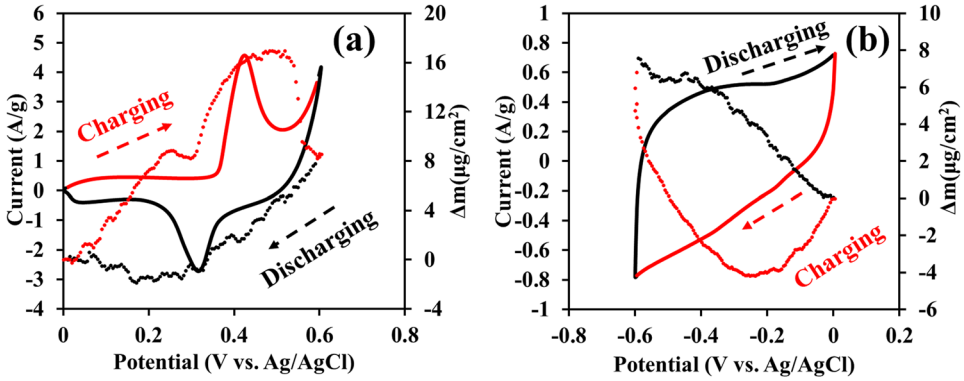

Figure 2. EQCM responses and CVs of (**a**) α-Ni(OH)$_2$-N-rGO$_{ae}$ and (**b**) N-rGO$_{ae}$ at 10 mVs^{-1}. Note, dash lines present the related mass changes of the electrodes during charging/discharging.

were subsequently coated on the top layer in Fig. 1b. Note, lower magnification FE-SEM images of CFP and the as-electrodeposited α-Ni(OH)$_2$ on CFP are displayed in Figure S1 and b, respectively. In addition, a *transmission electron microscopy* (TEM) image of N-rGO$_{ae}$ in Fig. 1c indicates a few layers of N-rGO$_{ae}$ sheets forming the wrinkle structure confirming the framework structure of the aerogel. This structure can address the restacking issue typically found in 2D graphene or rGO nanosheets. The interconnected porous structure can also deliver large surface area and porosity as well as great electrical conductivity. A TEM image of Ni(OH)$_2$-coated N-rGO$_{ae}$ sheets in Fig. 1d displays the dark Ni(OH)$_2$ particles with 25 nm in diameter dispersed on the N-rGO$_{ae}$ layers. Note, XRD, Raman, and XPS of Ni(OH)$_2$, N-rGO$_{ae}$ and Ni(OH)$_2$-N-rGO$_{ae}$ are shown in Figures S2 and S3 of the Supporting Information.

Charge storage mechanisms. The charge-discharge mechanisms of the α-Ni(OH)$_2$-N-rGO$_{ae}$ and N-rGO$_{ae}$ electrodes were investigated using the EQCM together with the CV technique. The CV of the α-Ni(OH)$_2$-coated N-rGO$_{ae}$ electrode is presented in Fig. 2a. The forward scan started from 0 to 0.6 V vs. Ag/AgCl for which an anodic peak occurs at 0.43 V vs. Ag/AgCl indicating that α-Ni(OH)$_2$ reacts with OH^- providing γ-NiOOH, a water molecule, and an electron through the oxidation[13–15]. Along this forward scan, the mass change (Δm) of the electrode is about 8.5 μg cm^{-2} owing to the insertion of solvated OH^- ions into α-Ni(OH)$_2$ interlayer separation. Also, the increasing Δm during the forward scan refers to the charging mechanism[28]. On the other hand, the backward scan (the discharging process) was swept back from 0.6 to 0 V vs. Ag/AgCl. The Δm of the electrode is reduced back to an original value, 0 μg cm^{-2} (see a black dash line in Fig. 2a) due to the full desertion of solvated OH^-. It can be concluded from the EQCM/CV results that the charge storage mechanism of the α-Ni(OH)$_2$-N-rGO$_{ae}$ is based on the interaction chemistry especially at slow scan rates. α-Ni(OH)$_2$-N-rGO$_{ae}$ is then considered as the battery-type electrode material.

For the N-rGO$_{ae}$ electrode, the CV and Δm vs. the applied potentials are shown in Fig. 2b. The CV with a working voltage of ca. 0.6 V exhibits a most likely rectangular shape representing a good EDLC behavior of the N-rGO$_{ae}$. Broad peaks also represent the redox reactions of N-containing groups[26,27]. For the charging process, the range of potential from 0 V to −0.6 V vs. Ag/AgCl was applied for which the Δm is decreased at a working window from 0 to −0.2 V vs. Ag/AgCl due to the desorption of ionic species initially adsorbed/absorbed when the electrode is immersed in the electrolytes without applying potential. This counter-ion desorption observed in this work is in good agreement with the new perspective charge storage mechanism recently proposed using *in situ* NMR[29]. At a potential range between −0.2 V and −0.6 V vs. Ag/AgCl, the Δm is rapidly increased to 7.5 μg cm^{-2} due to the adsorption/absorption of hydrated K^+ within the active pores of N-rGO$_{ae}$.

To confirm the charge storage behavior of the as-prepared α-Ni(OH)$_2$-N-rGO$_{ae}$ electrode, the *in situ* XAS technique was performed with the chronoamperometry in 1 M KOH electrolyte during applying the potentials stepped from 0.0, 0.35, 0.5 and 0.6 V vs. Ag/AgCl and the following backward scan at the applied potentials from 0.6, 0.4, 0.18 to 0 V vs. Ag/AgCl. Note, the Ni K-edge XANES of the samples were recorded and compared with Ni foil (Ni^0, 8333.00 eV), NiO (Ni^{2+}, 8345.20 eV) and $LaNiO_3$ (Ni^{3+}, 8348.20 eV) standards[30].

In Fig. 3a and b, the Ni K-edge fluorescence energy of the Ni(OH)$_2$-N-rGO$_{ae}$ electrode charged at 0.0 V vs. Ag/AgCl is 8345.25 eV ($Ni^{+2.26}$) and the adsorption energy remains constant at +2.26 until 0.35 V vs. Ag/AgCl before increasing to the energy value of 8347.84 ($Ni^{+2.76}$) and 8348.00 eV ($Ni^{+2.79}$) when the charging potentials were applied to 0.5 and 0.6 V vs. Ag/AgCl, respectively. This is due to the oxidation reaction of Ni(OH)$_2$ with OH^- providing NiOOH. This result further confirms the EQCM results. For the discharging process, the Ni K-edge fluorescence energy of the Ni(OH)$_2$-N-rGO$_{ae}$ electrode discharged at 0.4 V vs. Ag/AgCl is 8347.84 eV ($Ni^{+2.76}$) and continues to stable at 8345.25 eV ($Ni^{+2.26}$) when discharged at 0.18 V and 0 V vs. Ag/AgCl. These results also confirm the reversible redox reaction of Ni(OH)$_2$-N-rGO$_{ae}$ electrode.

Hybrid energy storage of Ni(OH)$_2$-N-rGO$_{ae}$//N-rGO$_{ae}$. The as-fabricated Ni(OH)$_2$-N-rGO$_{ae}$//N-rGO$_{ae}$ AES can provide a wide working potential (See Fig. 4a), which is greater than all aqueous-based Ni(OH)$_2$ symmetric supercapacitors[3,9,31]. Note, the total active material of the device is 4.0 mg consisting of 1.47 mg of Ni(OH)$_2$-N-rGO$_{ae}$ at the positive electrode and 2.53 mg of N-rGO$_{ae}$ at the negative electrode. In addition, the CV

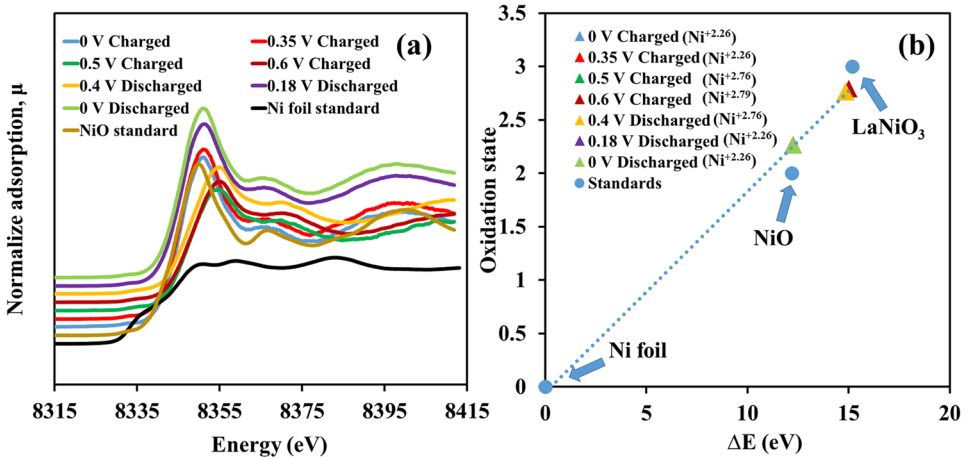

Figure 3. (**a**) *In situ* high-resolution Ni K-edge fluorescence XAS spectra of the as-prepared $Ni(OH)_2$-N-rGO_{ae} electrode and Ni standard compounds and (**b**) the oxidation states vs. ΔE (eV) of the $Ni(OH)_2$-N-rGO_{ae} electrode during charging/discharging by a chronoamperometry method at different applied potentials vs. Ag/AgCl.

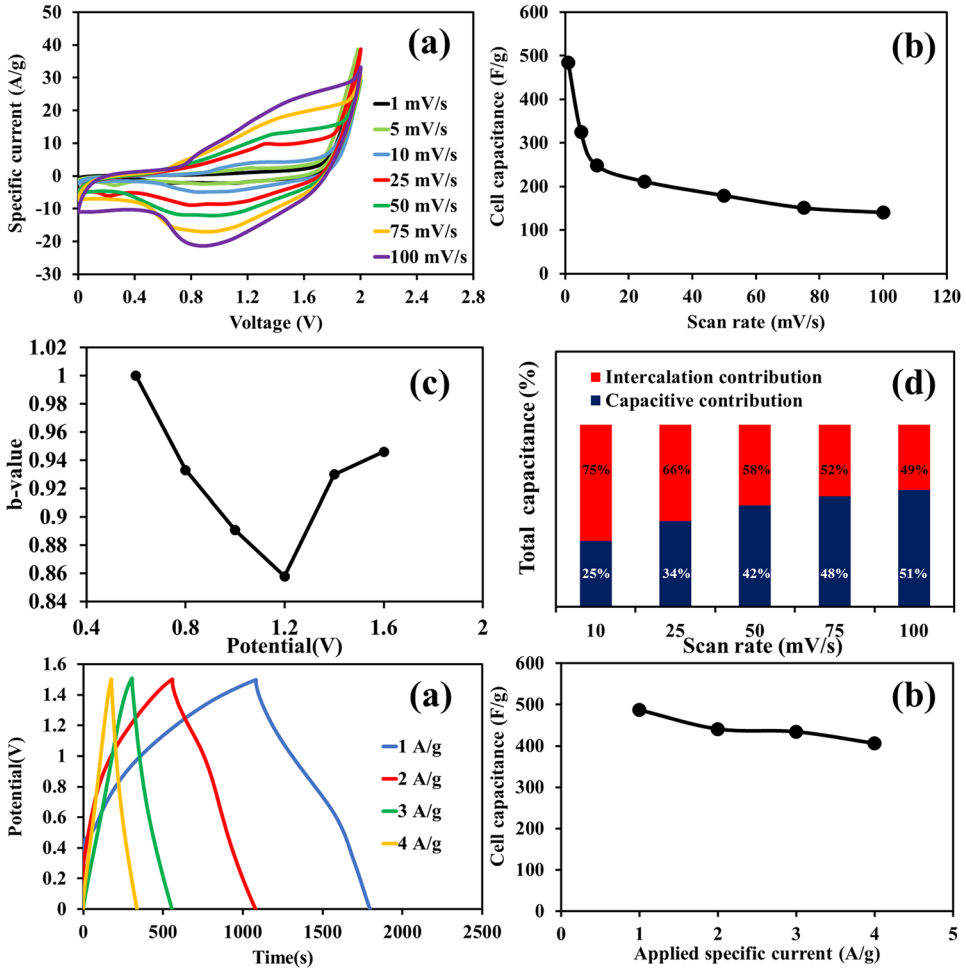

Figure 4. (**a**) CV curves at different scan rates, (**b**) specific capacitance vs. scan rate, (**c**) *b*-value vs. potential (V), (**d**) total capacitances at different scan rates, (**e**) GCD curves and (**f**) specific capacitance vs. applied currents of the $Ni(OH)_2$-N-rGO_{ae}//N-rGO_{ae} AES. Note, the total active material of the device is 4.0 mg consisting of 1.47 mg of $Ni(OH)_2$-N-rGO_{ae} at the positive electrode and 2.53 mg of N-rGO_{ae} at the negative electrode.

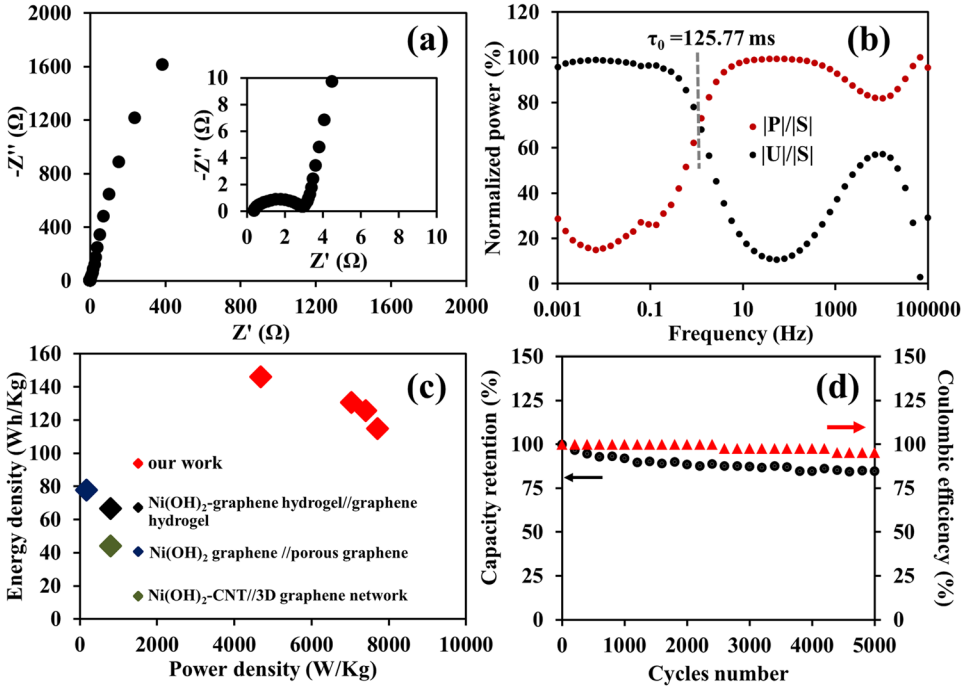

Figure 5. The electrochemical properties of the $Ni(OH)_2$-N-rGO_{ae}//N-rGO_{ae} AES: (**a**) Nyquist plot, (**b**) the plots of normalized power with the frequency, (**c**) maximum power density vs. energy density compared with some previous report[34,43,44] and (**d**) the capacity retention over 5000 cycles at 1 A g^{-1}.

shows the characteristics of the pseudocapacitors consisting of both capacitive and faradaic currents. The couple redox peaks are observed owing to the intercalation and deintercalation of the solvated $OH^-(H_2O)_n$ (*where* $n \geq 1$)[32]. Whilst, the capacitive current observed in the CVs is mostly due to the adsorption of hydrated K^+ on the N-rGO_{ae} negative electrode surface. The cell specific capacitances of the AES device are 484.3, 324.4, 247.8, 211.4, 179.1, 150.8 and 140.4 F g^{-1} at 1, 5, 10, 25, 50, 75 and 100 mV s^{-1}, respectively (Fig. 4b). From a power law, *b* value was then calculated[33], $i = av^b$ where the current is represented as *i* and the scan rate is represented as *v*. The adjustable parameters are expressed as *a* and *b*. Typically, the *b* value is equal to 1.0 for non-diffusion-controlled surface capacitive (an EDLC-like electrochemical feature) and equal to 0.5 for diffusion-controlled redox reaction, which is a typical battery behavior[19,34]. From the beginning, the *b* value of the cell device is almost amounted to 1 before dropping down to 0.86 (see Fig. 4c) indicating that the specific capacitances of the device are contributed from both diffusion-controlled battery-type behavior and capacitive effect. The capacitive contribution fraction at different scan rates can be examined from $i(V) = k_1 v + k_2 v^{0.5}$ where k_1 and k_2 are alterable parameters determined from the slope and y-axis intercept of the plots between $i(V)$ and *v*, respectively. The capacitive and intercalation contribution fractions are shown in Fig. 4d. It is clearly observed that they are sensitive to scan rates. In addition to the CV results, GCD curves were carried out and shown in Fig. 4e for which the shapes of the charge and discharge curves imply good conductivity, excellent coulombic efficiency and high electrochemical reversibility of the AES. Besides, the calculated cell capacitances are 487.1, 441.1, 434.5 and 406.5 F g^{-1} at 1, 2, 3 and 4 A g^{-1}, respectively (see Fig. 4f). The actual working potential window excluding the *iR* drop is ca. 1.5 V. When compared with other previous report, the as-fabricated $Ni(OH)_2$-N-rGO_{ae}//N-rGO_{ae} AES exhibits significantly higher specific capacitance than other $Ni(OH)_2$-based asymmetric supercapacitors (see Table S1 of the Supporting Information).

The electrochemical impedance spectroscopy (EIS) of the as-fabricated AES was eventually performed by applying a sinusoidal signal of 10 mV amplitude from 1 mHz to 100 kHz. The bottom left-hand corner of the Nyquist plot in Fig. 5a shows a high frequency result for which 2.6 Ω of the charge transfer resistance (R_{ct}) due to the redox reaction and 0.4 Ω of the internal resistance (R_s) are observed. Note, the R_s here is rather small when compared with the other previous work[35]. To further investigate the power efficiency of the as-fabricated AES, the relaxation time (τ_0), which is the minimum time required for discharging the stored charges from the AES, was determined and shown in Fig. 5b. The smaller τ_0 represents the higher power efficiency of the AES[36]. The response of frequency (f_0), which is corresponding to the maximum point energy curve, is estimated to be at 1.26 Hz. The determined τ_0, which is equal to $1/2\ \pi f_0$, is 125.77 ms indicating that the as-fabricated AES can provide a quick discharging process and also substantially faster than other previous report[35]. Remarkably, the device can display a high specific energy of 146 Wh kg^{-1} at a specific power of 4687 W kg^{-1} with the remaining of 115 Wh Kg^{-1} at 7705 W kg^{-1} (Fig. 5c). The highest specific energy here is much greater than 77.8 Wh kg^{-1} of the asymmetric supercapacitor of the $Ni(OH)_2$-graphene//graphene[4] and significantly higher than 35.7 Wh kg^{-1} of the amorphous $Ni(OH)_2$ supercapacitor[6]. The as-fabricated AES provides high capacity retention over 84.61% after 5000 cycles (see Fig. 5d). This number is rather high when compared with NiCd and NiMH batteries and

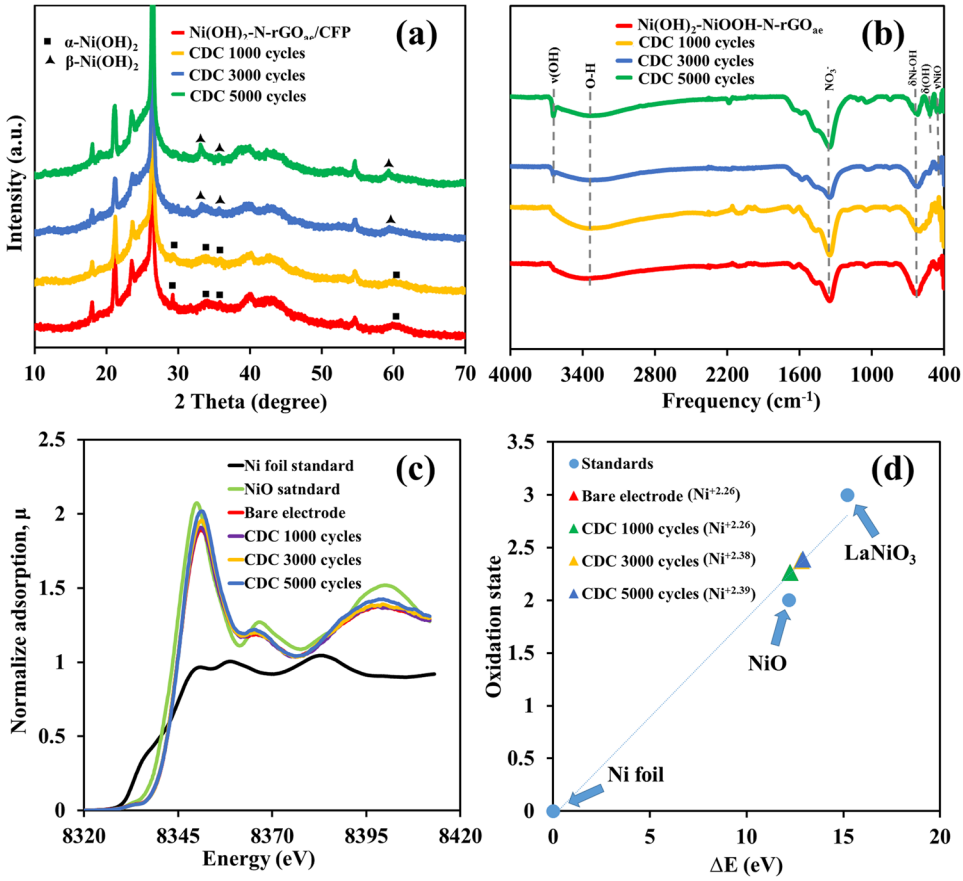

Figure 6. (**a**) XRD patterns and (**b**) FTIR spectra of the $Ni(OH)_2$-N-rGO_{ae}/CFP electrodes after charged/discharged as well as (**c**) *ex situ* high-resolution XAS spectra and (**d**) the oxidation states vs. ΔE (eV) of the $Ni(OH)_2$-N-rGO_{ae} after 1000, 3000 and 5000 cycles as compared with the Ni standard compounds.

other $Ni(OH)_2$-based supercapacitors[6]. As the result, the $Ni(OH)_2$-N-rGO_{ae}//N-rGO_{ae} is ideally suitable for many high power and energy applications.

***Ex situ* evaluation of the AES device.** After the AES devices were electrochemically tested, *ex situ* measurements of the disassembled positive electrodes were carried out by XRD, FTIR, XAS and XPS. The XRD results in Fig. 6a can imply that α-$Ni(OH)_2$ on the positive electrode after tested begins to convert to β-$Ni(OH)_2$ after 3000 cycles. Additionally, XRD patterns of β-$Ni(OH)_2$ with the diffraction peaks (100), (101), and (110), are initially witnessed on the XRD patterns of the $Ni(OH)_2$-N-rGO_{ae} after 3000 cycles. The calculated interlayer spacing is reduced from 7.00 Å (α-$Ni(OH)_2$, JCPDS 38–715) to 4.45 Å (β-$Ni(OH)_2$, JCPDS 14–0117). The less interlayer spacing can obstruct the diffusion of the $OH^-(H_2O)_n$ (where $n \geq 1$) clusters to the $Ni(OH)_2$ layers. To further investigate the phase transformation of α-$Ni(OH)_2$ to β -$Ni(OH)_2$ after long cycling, the $Ni(OH)_2$-N-rGO_{ae} electrodes after tested at 1000, 3000 and 5000 cycles were investigated by FTIR and XPS techniques (see FTIR in Fig. 6b and XPS in Figure S5). In addition, *ex situ* XAS was applied to investigate the oxidation number of Ni element in the positive electrodes of the AESs after 1000, 3000 and 5000 cycles. The XANES spectra and oxidation state for each sample are shown in Fig. 6c and d, respectively. The Ni K-edge XANES of the samples was recorded and compared with Ni foil (Ni^{+0}, 8333 eV), NiO (Ni^{+2}, 8345.20 eV) and $LaNiO_3$ (Ni^{3+}, 8348.20 eV) standards[30]. The adsorption edge energy of Ni on the electrode and after tested for 1000, 3000, 5000 cycles are 8345.25 eV ($Ni^{+2.26}$), 8345.84 eV ($Ni^{+2.38}$) and 8345.91 eV ($Ni^{+2.39}$), respectively. These results indicate that the $Ni(OH)_2$ phase begins to transform after 3000 cycles. After 5000 cycles, the phase of α-$Ni(OH)_2$ is completely changed to β-$Ni(OH)_2$. When the interlayer distance is decreased, the charge mechanism does no longer follow the reversible reaction (1) anymore, the β-$Ni(OH)_2$ phase will get oxidized and turned to β-NiOOH rather than γ-NiOOH (see Figure S6) leading to poor capacity retention typically detected in the α-$Ni(OH)_2$-based AESs. The reaction mechanism is shown in details in Figure S6 of the supporting information.

Conclusions

N-rGO_{ae} was produced from GO through a hydrothermal reduction with hydrazine and coated on the CFP via a spray-coating technique. α-$Ni(OH)_2$ was coated on the N-rGO_{ae} substrate by an electrodeposition using a chronoamperometry at −0.9 V vs Ag/AgCl for 5 min. The charge storage mechanism of α-$Ni(OH)_2$-coated N-rGO_{ae} was investigated by *in situ* EQCM and XAS. The mass change of the positive electrode during the

charging/discharging processes determined by the EQCM is about 8.5 μg cm^{-2} owing to the insertion/desertion of solvated OH^- ions into the interlayer spacing of α-$Ni(OH)_2$. At the negative electrode, the EQCM shows that the mass change of the solvated K^+ electrolytes, physically adsorbed/desorbed to the N-rGO_{ae} electrode via the EDLC mechanism, is 7.5 μg cm^{-2} during the charging/discharging processes. The Ni oxidation state of the $Ni(OH)_2$-N-rGO_{ae} electrode after charged at 0.0 V vs. Ag/AgCl is +2.26 and remained stable at this oxidation state until 0.35 V vs. Ag/AgCl before oxidized to +2.76 and +2.79 after charged at 0.5 and 0.6 V vs. Ag/AgCl, respectively. This is due to the oxidation reaction of $Ni(OH)_2$ with OH^- providing NiOOH. For the discharging process, the Ni oxidation state of the $Ni(OH)_2$-N-rGO_{ae} electrode is reduced back to +2.76 after discharged at 0.4 V vs. Ag/AgCl and +2.26 at 0 V vs Ag/AgCl. These results show good reversible redox reaction of the $Ni(OH)_2$-N-rGO_{ae} electrode. A single coin-cell AES of $Ni(OH)_2$-N-rGO_{ae}//N-rGO_{ae} (CR2016) was assembled using a hydrolyzed polyethylene separator absorbed with 1 M KOH. The as-fabricated energy storage can provide a wide working voltage of 1.5 V with a high specific energy of 146 Wh kg^{-1} and a maximum specific power of 7705 W kg^{-1} with 84.61% capacity retention after 5000 cycles. Interestingly, after 3000 cycles, the α-$Ni(OH)_2$, which has a wide interlayer separation of 7.0 Å, was partially changed to β-$Ni(OH)_2$, which has a narrower interlayer separation of 4.45 Å. This leads to the capacity retention decay since the β-$Ni(OH)_2$ has too narrow interlayer spacing for the solvated electrolytes, $OH^-(H_2O)n$ where $n \geq 1$. This energy storage device has a potential to be used in high energy and power applications. Also, this device has a bright potential to replace the NiCd and NiMH technologies since we do not need toxic Cd and expensive La alloy at the negative electrode.

Experimental Section

Synthesis of nitrogen-doped reduced graphene oxide (N-rGO_{ae}). A hydrothermal reduction method was used to synthesize N-rGO_{ae}. Briefly, 3 mg/ml of GO from the modified Hummers method[26, 37–39] was prepared in Milli-Q water using ultrasonication for 30 min. 0.5 M hydrazine hydrate (N_2H_4, 80% Merck) was added to the mixture, and then the suspension was poured into a Teflon-lined autoclave and heated at 100 °C for 3 h. After naturally cooling down the autoclave to room temperature, a vacuum filtration is used to collect the N-rGO hydrogel. The as-filtrated N-rGO hydrogel was left in Milli-Q water at 25 °C and the water was daily replaced for washing out the remaining of reducing agent. After that the hydrogel was frozen at 0 °C for 24 h. Then, the frozen hydrogel was put in a freezing dryer to remove water at −55 °C for 72 h to form the final product N-rGO_{ae}. Next, a spray coating technique is applied using an airbrush with 0.3 mm of brush nozzle (Paasche Airbrush Company, USA) to coat the N-rGO_{ae} on the CFP (Carbon fiber paper) surface at 20 psi and room temperature. Finally, the electrode was dried in vacuum oven at 60 °C for 24 h[40].

Electrodeposition of nickel hydroxide (α-$Ni(OH)_2$) on N-rGO_{ae} electrode. Firstly, α-$Ni(OH)_2$ was deposited on the N-rGO_{ae}-coated CFP substrate by applying −0.9 V vs. Ag/AgCl for 5 min through a chronoamperometry method using a Metrohm AUTOLAB potentiostat (PGSTAT 302 N made in Netherlands running NOVA version 1.10.3 software). The electrodeposition solution (60 ml) is 0.1 M nickel (II) nitrate hexahydrate ($Ni(NO_3)_2.6H_2O$, 97% QRec) in 0.5 M sodium nitrate ($NaNO_3$, 99.5% QRec). The counter electrode is the platinum wire and the reference electrode is the Ag/AgCl (3 M KCl). After electrodeposition process, the as-electrodeposited α-$Ni(OH)_2$ (0.97 mg) on the 0.5-mg N-rGO_{ae}-coated CFP substrate was rinsed 5 times using Milli-Q water before putting into a vacuum dryer at 50 °C overnight to dry off the samples.

Material characterizations. Field-emission scanning electron microscopy (FE-SEM, JSM-7001F (JEOL Ltd., Japan)) and transmission electron microscopy (TEM, JEM 1220 (JEOL Ltd., Japan)) were applied to study the morphologies of the as-prepared materials. The structures of the materials were examined by X-ray diffraction (XRD, Bruker optics, Germany) using a monochromatic Cu Kα radiation ($\lambda = 0.15405$ nm), Fourier Transform Infrared Spectrometer (FT-IR, PerkinElmer Paragon 1000) and Raman spectroscopy (Senterra Dispersive Raman Microscope, Bruker) with an excitation wavelength of 532 nm. The chemical composition on the surface of the materials was characterized by X-ray photoelectron spectroscopy (XPS, Axis Ultra DLD, Kratos Analytical Ltd) with Al-K alpha radiation ($h\upsilon = 14{,}866$ eV).

For X-ray absorption spectroscopy (XAS) measurement, Ni K-edge fluorescent XAS was performed at a beamline No. 5.2 at the Synchrotron Light Research Institute (Public Organization), Nakhon Ratchasima, Thailand. The Ge(220) double-crystal monochromator (energy range 3440–12100 eV) is used and a fluorescence mode with a 4-element silicon drift detector, which was placed 90° to the beam and 45° to the sample, is applied to record the spectroscopic data. The Ni K-edge (8333 eV) was calibrated using the Ni foil before measurement. The light dimension on the sample was adjusted to 5 mm width and 1 mm height.

The charge storage mechanism of $Ni(OH)_2$-N-rGO_{ae} electrode was studied through the *in situ* XAS technique together with the chronoamperometry in 1 M KOH electrolyte by applying the potentials stepped from 0.0, 0.35, 0.5 to 0.6 V vs. Ag/AgCl following by the backward process from 0.6, 0.4, 0.18 to 0 V vs. Ag/AgCl. For reaching the steady state, each step potential was hold for 15 min before starting the XAS measurement[41, 42]. Additionally, acrylic sheets, which are used as the materials of the electrochemical cell, has a dimension of $2 \times 2 \times 3.5$ cm^3 with a drilled hole diameter of 1 cm on one 2-cm^2 side of the acrylic sheet. The drilled hole was covered by a larger piece of polypropylene film. During the process for measuring, the Ag/AgCl in 3 M KCl (reference electrode) and Pt wire (counter electrode) were located near the $Ni(OH)_2$-N-rGO_{ae} electrode at a distance of ca.1 cm. The *ex situ* Ni K-edge XAS was also carried out in the fluorescence mode.

Fabrication of AES and the electrochemical evaluation. The AES was assembled of the negative and positive electrodes with a geometrical coin cell (CR2016). Hydrolyzed polyethylene (PE) film with a thickness of 25 μm, which was used as the separator, was soaked in 1 M KOH for 10 min before used. Then, the separator was inserted between the positive electrode (1.47-mg $Ni(OH)_2$-N-rGO_{ae} coated on CFP) and the negative electrode

(2.53-mg N-rGO$_{ae}$ coated on CFP). Finally, the coin cell was then assembled by pressing with a crimper machine at 100 psi. The charge storage mechanism was performed by the EQCM technique via a cyclic voltammetry (CV) combining with quartz crystal microbalance techniques of Au/TiO_2. The EQCM electrode was tested in atmospheric pressure and at room temperature (25 °C) using a three-electrode system; Ag/AgCl (3 M KCl in gel) as a reference electrode and Au spiral shape as a counter electrode. The electrochemical property of the as-fabricated supercapacitors was evaluated by CV, galvanostatic charge–discharge (GCD), and electrochemical impedance spectroscopy (EIS) using a Metrohm AUTOLAB potentiostat (PGSTAT 302 N) made in Netherlands running NOVA software (version 1.11).

References

1. Bode, H., Dehmelt, K. & Witte, J. Zur kenntnis der nickelhydroxidelektrode—I.Über das nickel (II)-hydroxidhydrat. *Electrochim. Acta* **11**, 1079–1087 (1966).
2. Hall, D. S., Lockwood, D. J., Bock, C. & MacDougall, B. R. Nickel hydroxides and related materials: a review of their structures, synthesis and properties. *Proc. R. Soc. A* **471**, 20140792, doi:10.1098/rspa.2014.0792 (2015).
3. Wang, H., Casalongue, H. S., Liang, Y. & Dai, H. Ni(OH)$_2$ Nanoplates Grown on Graphene as Advanced Electrochemical Pseudocapacitor Materials. *J. Am. Chem. Soc.* **132**, 7472–7477 (2010).
4. Yan, J. *et al.* Advanced asymmetric supercapacitors based on Ni(OH)$_2$/graphene and porous graphene electrodes with high energy density. *Adv. Funct. Mater.* **22**, 2632–2641 (2012).
5. Hu, C. C., Chen, J. C. & Chang, K. H. Cathodic deposition of Ni(OH)$_2$ and Co(OH)$_2$ for asymmetric supercapacitors: Importance of the electrochemical reversibility of redox couples. *J. Power Sources* **221**, 128–133 (2013).
6. Li, H. B. *et al.* Amorphous nickel hydroxide nanospheres with ultrahigh capacitance and energy density as electrochemical pseudocapacitor materials. *Nat. Commun.* **4**, doi:10.1038/ncomms2932 (2013).
7. Boruah, B. D. & Misra, A. Nickel hydroxide coated carbon nanoparticles mediated hybrid three-dimensional graphene foam assembly for supercapacitor. *RSC Adv.* **6**, 36307–36313 (2016).
8. Zhu, Y. Q. *et al.* Ultrathin Nickel Hydroxide and Oxide Nanosheets: Synthesis, Characterizations and Excellent Supercapacitor Performances. *Sci. Rep.* **4**, doi:10.1038/srep05787 (2014).
9. Yang, G.-W., Xu, C.-L. & Li, H.-L. Electrodeposited nickel hydroxide on nickel foam with ultrahigh capacitance. *Chem. Commun.*, 6537–6539 (2008).
10. Chen, Y. *et al.* Enhanced Structural Stability of Nickel–Cobalt Hydroxide via Intrinsic Pillar Effect of Metaborate for High-Power and Long-Life Supercapacitor Electrodes. *Nano Lett.* **17**, 429–436 (2017).
11. Liu, Y., Wang, R. & Yan, X. Synergistic effect between ultra-small nickel hydroxide nanoparticles and reduced graphene oxide sheets for the application in high-performance asymmetric supercapacitor. *Sci. Rep.* **5**, doi:10.1038/srep11095 (2015).
12. Hu, G., Li, C. & Gong, H. Capacitance decay of nanoporous nickel hydroxide. *J. Power Sources* **195**, 6977–6981 (2010).
13. Kamath, P. V. *et al.* Stabilized α-Ni(OH)$_2$ as Electrode Material for Alkaline Secondary Cells. *J. Electrochem. Soc.* **141**, 2956–2959 (1994).
14. Singu, B. S. & Yoon, K. R. Porous 3D-β-nickel hydroxide microflowers for electrochemical supercapacitors. *J. Ind. Eng. Chem.* **33**, 374–380 (2016).
15. Liu, Y., Wang, R. & Yan, X. Synergistic Effect between Ultra-Small Nickel Hydroxide Nanoparticles and Reduced Graphene Oxide sheets for the Application in High-Performance Asymmetric Supercapacitor. *Sci. Rep.* **5**, 11095, doi:10.1038/srep11095 (2015).
16. Li, B., Ai, M. & Xu, Z. Mesoporous [small beta]-Ni(OH)$_2$: synthesis and enhanced electrochemical performance. *Chem. Commun.* **46**, 6267–6269 (2010).
17. Wu, Z. *et al.* Electrostatic Induced Stretch Growth of Homogeneous β-Ni(OH)$_2$ on Graphene with Enhanced High-Rate Cycling for Supercapacitors. *Sci. Rep.* **4**, 3669, doi:10.1038/srep03669 (2014).
18. Gogotsi, Y. What Nano Can Do for Energy Storage. *ACS Nano* **8**, 5369–5371 (2014).
19. Simon, P., Gogotsi, Y. & Dunn, B. Where Do Batteries End and Supercapacitors Begin? *Science* **343**, 1210–1211 (2014).
20. Yang, S. *et al.* Spherical [small alpha]-Ni(OH)$_2$ nanoarchitecture grown on graphene as advanced electrochemical pseudocapacitor materials. *Chem. Commun.* **48**, 2773–2775 (2012).
21. Lee, J. W., Ahn, T., Soundararajan, D., Ko, J. M. & Kim, J.-D. Non-aqueous approach to the preparation of reduced graphene oxide/[small alpha]-Ni(OH)$_2$ hybrid composites and their high capacitance behavior. *Chem. Commun.* **47**, 6305–6307 (2011).
22. Sun, X. *et al.* Morphology controlled high performance supercapacitor behaviour of the Ni–Co binary hydroxide system. *J. Power Sources* **238**, 150–156 (2013).
23. Wu, Z.-S. *et al.* Synthesis of Graphene Sheets with High Electrical Conductivity and Good Thermal Stability by Hydrogen Arc Discharge Exfoliation. *ACS Nano* **3**, 411–417 (2009).
24. Fan, W., Miao, Y.-E., Huang, Y., Tjiu, W. W. & Liu, T. Flexible free-standing 3D porous N-doped graphene-carbon nanotube hybrid paper for high-performance supercapacitors. *RSC Adv.* **5**, 9228–9236 (2015).
25. Shan, D., Yang, J., Liu, W., Yan, J. & Fan, Z. Biomass-derived three-dimensional honeycomb-like hierarchical structured carbon for ultrahigh energy density asymmetric supercapacitors. *J. Mater. Chem. A* **4**, 13589–13602 (2016).
26. Iamprasertkun, P., Krittayavathananon, A. & Sawangphruk, M. N-doped reduced graphene oxide aerogel coated on carboxyl-modified carbon fiber paper for high-performance ionic-liquid supercapacitors. *Carbon* **102**, 455–461 (2016).
27. Krittayavathananon, A., Iamprasertkun, P. & Sawangphruk, M. Enhancing the charge-storage performance of N-doped reduced graphene oxide aerogel supercapacitors by adsorption of the cationic electrolytes with single-stand deoxyribonucleic acid. *Carbon* **109**, 314–320 (2016).
28. Tsai, W.-Y., Taberna, P.-L. & Simon, P. Electrochemical Quartz Crystal Microbalance (EQCM) Study of Ion Dynamics in Nanoporous Carbons. *J. Am. Chem. Soc.* **136**, 8722–8728 (2014).
29. Griffin, J. M. *et al. In situ* NMR and electrochemical quartz crystal microbalance techniques reveal the structure of the electrical double layer in supercapacitors. *Nat. Mater.* **14**, 812–819 (2015).
30. Woolley, R. J., Illy, B. N., Ryan, M. P. & Skinner, S. J. *In situ* determination of the nickel oxidation state in La_2NiO^{4+} and $La_4Ni_3O_{10}$ using X-ray absorption near-edge structure. *J. Mater. Chem.* **21**, 18592–18596 (2011).
31. Songzhan, L. *et al. In situ* synthesis of 3D CoS nanoflake/Ni(OH)$_2$ nanosheet nanocomposite structure as a candidate supercapacitor electrode. *Nanotechnol* **27**, 145401 (2016).
32. Tuckerman, M. E., Marx, D. & Parrinello, M. The nature and transport mechanism of hydrated hydroxide ions in aqueous solution. *Nature* **417**, 925–929 (2002).
33. Sathiya, M., Prakash, A. S., Ramesha, K., Tarascon, J. M. & Shukla, A. K. V2O5-Anchored Carbon Nanotubes for Enhanced Electrochemical Energy Storage. *J. Am. Chem. Soc.* **133**, 16291–16299 (2011).
34. Wang, R., Xu, C. & Lee, J.-M. High performance asymmetric supercapacitors: New NiOOH nanosheet/graphene hydrogels and pure graphene hydrogels. *Nano Energ.* **19**, 210–221 (2016).
35. Ganesh, V., Pitchumani, S. & Lakshminarayanan, V. New symmetric and asymmetric supercapacitors based on high surface area porous nickel and activated carbon. *J. Power Sources* **158**, 1523–1532 (2006).
36. Zhang, S. & Pan, N. Supercapacitors Performance Evaluation. *Adv. Energ. Mater.* **5**, n/a–n/a, doi:10.1002/aenm.201401401 (2015).

37. Sanguansak, Y. *et al.* Permselective properties of graphene oxide and reduced graphene oxide electrodes. *Carbon* **68**, 662–669 (2014).
38. Hummers, W. S. & Offeman, R. E. Preparation of Graphitic Oxide. *J. Am. Chem. Soc.* **80**, 1339–1339 (1958).
39. Sawangphruk, M., Srimuk, P., Chiochan, P., Sangsri, T. & Siwayaprahm, P. Synthesis and antifungal activity of reduced graphene oxide nanosheets. *Carbon* **50**, 5156–5161 (2012).
40. Suktha, P. *et al.* High-Performance Supercapacitor of Functionalized Carbon Fiber Paper with High Surface Ionic and Bulk Electronic Conductivity: Effect of Organic Functional Groups. *Electrochim. Acta* **176**, 504–513 (2015).
41. Wongsaprom, K., Sonsupap, S., Maensiri, S. & Kidkhunthod, P. Room-temperature ferromagnetism in Fe-doped In2O3 nanoparticles. *App. Phys. A* **121**, 239–244 (2015).
42. Daengsakul, S. *et al.* The effect of Gd doping in La1−x−yGdxSryMnO3 compound on nanocrystalline structure by X-ray Absorption Spectroscopy (XAS) technique. *Microelectron. Eng.* **146**, 38–42 (2015).
43. Yan, J. *et al.* Advanced Asymmetric Supercapacitors Based on $Ni(OH)_2$/Graphene and Porous Graphene Electrodes with High Energy Density. *Adv. Funct. Mater.* **22**, 2632–2641 (2012).
44. Yi, H. *et al.* Advanced asymmetric supercapacitors based on CNT@$Ni(OH)_2$ core-shell composites and 3D graphene networks. *J. Mater. Chem. A* **3**, 19545–19555 (2015).

Acknowledgements

This work was financially supported Thailand Research Fund and Vidyasirimedhi Institute of Science and Technology (RSA5880043). P. Sirisinudomkit appreciated the financial support (M. Eng. Scholarship) from the Faculty of Engineering and the National Research University Project of Thailand (NRU) at Kasetsart University. Synchrotron Light Research Institute (Public Organization), Thailand for XPS and XAS facilities.

Author Contributions

M.S. conceived and designed this work and wrote the paper; P.S. carried out the experiment, and P.I., A.K. and T.P. performed XAS and EQCM. All authors participated in the analysis and discussion of the results.

Additional Information

Supplementary information accompanies this paper at doi:10.1038/s41598-017-01191-8

Competing Interests: The authors declare that they have no competing interests.

Publisher's note: Springer Nature remains neutral with regard to jurisdictional claims in published maps and institutional affiliations.